




# Double-peaked Pulse Profile of FRB 200428: Synchrotron Maser Emission from Magnetized Shocks Encountering a Density Jump

Di Xiao<sup>1,2</sup>  and Zi-Gao Dai<sup>1,2</sup><sup>1</sup> School of Astronomy and Space Science, Nanjing University, Nanjing 210023, People's Republic of China; [dxiao@nju.edu.cn](mailto:dxiao@nju.edu.cn), [dzg@nju.edu.cn](mailto:dzg@nju.edu.cn)<sup>2</sup> Key Laboratory of Modern Astronomy and Astrophysics (Nanjing University), Ministry of Education, People's Republic of China

Received 2020 September 30; revised 2020 October 23; accepted 2020 October 28; published 2020 November 19

## Abstract

Very recently a fast radio burst (FRB) 200428 associated with a strong X-ray burst from the Galactic magnetar SGR 1935+2154 was detected; this provides direct evidence supporting the magnetar progenitor models of FRBs. Assuming that the FRB radiation mechanism is synchrotron maser emission from magnetized shocks, we develop a specific scenario by introducing a density-jump structure of upstream medium, thus making the double-peaked character of FRB 200428 a natural outcome. The luminosity and emission frequency of two pulses can be well explained in this scenario. Furthermore, we find that the synchrotron emission of shock-accelerated electrons is in the X-ray band, and therefore can be responsible for at least a portion of observed X-ray fluence. With the proper upgrade, in the future this density-jump scenario could be applied to FRBs with multiple peaks.

*Unified Astronomy Thesaurus concepts:* [Radio transient sources \(2008\)](#); [Neutron stars \(1108\)](#); [Magnetars \(992\)](#)

## 1. Introduction

Fast radio bursts (FRBs) are bright millisecond radio pulses that flash randomly in the universe. The first FRB was discovered in 2007 (Lorimer et al. 2007); to date, hundreds of FRBs have been reported (Petroff et al. 2016). Many aspects of FRBs remain mysterious, especially their origin (for reviews, see Katz 2018; Popov et al. 2018; Cordes & Chatterjee 2019; Petroff et al. 2019). Tens of progenitor models have been proposed (see Platts et al. 2019 for a theory catalog), most of which involve compact objects that have been modeled according to the energetics and temporal variability of FRBs. Recently, a few observational breakthroughs have been made, which help us to better understand this phenomenon. The localization of 10 FRBs has been confirmed, and their host galaxies being identified (Tendulkar et al. 2017; Bannister et al. 2019; Prochaska et al. 2019; Ravi et al. 2019; Chittidi et al. 2020; Macquart et al. 2020; Marcote et al. 2020). The fact that some FRBs are located in the outskirts of host galaxies suggests that their progenitors are neutron stars (NSs). The periodic activity of two FRBs has been identified (CHIME/FRB Collaboration et al. 2020; Cruces et al. 2020; Rajwade et al. 2020), which also seems to favor this hypothesis. Moreover, to date approximately 20 FRBs have been found to repeat (CHIME/FRB Collaboration et al. 2019a, 2019b; Fonseca et al. 2020), implying that they require sustainable energy reservoirs. It has been suggested that, in these cases, young flaring magnetars could play this role (Popov & Postnov 2013; Lyubarsky 2014; Murase et al. 2016; Beloborodov 2017; Waxman 2017).

The above conjecture is supported by the detection in 2020 of FRB 200428 from the Galactic magnetar SGR 1935+2154 (Bochenek et al. 2020; The CHIME/FRB Collaboration et al. 2020). At nearly the same time, an associated X-ray burst was observed by the *Insight*-Hard X-ray Modulation Telescope (HXMT), INTERNATIONAL GAMMA-RAY ASTROPHYSICS LABORATORY (INTEGRAL), KONUS-WIND, and ASTRO RIVELATORE GAMMA A IMMAGINI LEGGERO (AGILE; Li et al. 2020; Mereghetti et al. 2020; Ridnaia et al. 2020; Tavani et al. 2020). This landmark discovery directly verified the fact that magnetars are

progenitors of at least a portion of FRBs. SGR 1935+2154 is a typical magnetar with spin period  $\sim 3.24$  s and surface magnetic field strength  $\sim 2.2 \times 10^{14}$  G (Israel et al. 2016). Several measurements of its distance give different values, within the range of 4.4–12.5 kpc (Koches et al. 2018; Mereghetti et al. 2020; Zhou et al. 2020; Zhong et al. 2020). FRB 200428 has two narrow pulses separated by  $\Delta T = 28.91$  ms. The first pulse was detected only by Canadian Hydrogen Intensity Mapping Experiment (CHIME), and the second was detected simultaneously by CHIME and the Survey for Transient Astronomical Radio Emission 2 (STARE2). Moreover, the first pulse cuts off quickly beyond 550 MHz, while the second pulse spans from 500 MHz up to 1468 MHz. The combined total fluence of the second pulse is at least 10 times higher than the first one. All these properties need to be addressed properly in a detailed theoretical model.

The radiation mechanism of FRBs is still largely unknown. The high brightness temperature implies that the radiation must be coherent. Generally there are three kinds of astrophysical approaches to the generation of coherence: coherent curvature emission by bunches, plasma emission by reactive instabilities, and maser emission (for a review, see Melrose 2017). In this work, we mainly consider the synchrotron maser mechanism by magnetized shocks, which was first proposed in the early 1990s. Bunching in the gyration phase of incoming particles near shock front has been verified by particle-in-cell (PIC) simulations (Hoshino & Arons 1991; Hoshino et al. 1992; Amato & Arons 2006; Plotnikov & Sironi 2019). The distribution of the particles in momentum space can be described as a cold ring form (Alsop & Arons 1988), which is beneficial for the development of synchrotron maser instability. The growth of electromagnetic (EM) waves can be very effective, and thus a maser (FRB) can be produced (Hoshino & Arons 1991). In this scenario, the physical condition of the shock upstream medium could have a major impact on observed FRB properties. For instance, Metzger et al. (2019) and Beloborodov (2020) assumed a slow ion tail of flare ejecta and magnetar wind as the upstream medium, respectively, therefore their predictions are different in many ways. This motivates us to study the influence on FRB

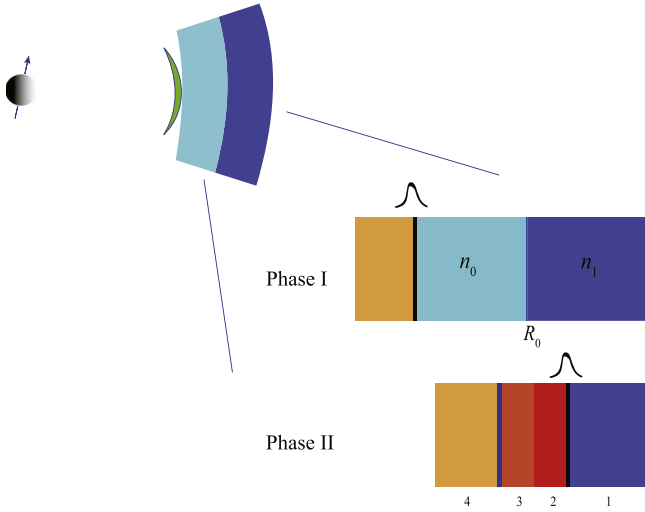


**Figure 1.** Schematic picture of our density-jump scenario. An ultra-relativistic ejecta from a magnetar flare collides with the leftover baryonic shell of previous flares. The shell is stratified, and the outer part is denser ( $n_0 < n_1$ ). The deceleration of the ejecta will go through two phases and two FRB pulses are produced via synchrotron maser emission near the forward shock front (marked by the thick black line).

emission if a density structure of external medium does exist. More intriguingly, recently Kirsten et al. (2020) reported a repetition of FRB 200428 with a double-peaked character after long-term monitoring, which supports our hypothesis of a stratified medium.

This Letter is organized as follows. We introduce the density-jump scenario in Section 2. In Section 3 we discuss the dynamics and constrain the density properties from the radio observation. Then the post-shock high-energy emission is discussed in Section 4. We finish with discussion and conclusions in Section 5.

## 2. Density Jump Scenario

The matter ejected during magnetar flares usually consists of two components: a relativistic ejecta and a subrelativistic baryonic shell. The shell could possibly have some structure due to unsteady ejection. For instance, Beloborodov (2020) suggested a distribution of ejected mass over velocity  $m(v) \propto v^\xi$  with  $\xi > 0$ , which implies an increasing density gradient with radius. In this work, the radial density profile is simplified as a jump between two constant densities, which is written as

$$n(r) = \begin{cases} n_0, & r < R_0, \\ n_1, & r \geq R_0, \end{cases} \quad (1)$$

where  $n_0 < n_1$  is assumed. Similar to Metzger et al. (2019), the relativistic ejecta collides with the baryonic shell characterized by Equation (1) from the previous flare. This scenario is illustrated in Figure 1.

The dynamic evolution of the system goes through two phases. In Phase I, forward and reverse shocks are formed when the ejecta collides with the inner shell. The reverse shock crosses the ejecta in a time  $t_{\text{cr},1} \simeq \delta t$  (Sari & Piran 1995), where  $\delta t$  is the flare duration. The first pulse of FRB 200428 is probably produced via synchrotron maser emission at the crossing radius, where both the luminosity and energy of the forward shock is at its maximum. After  $t_{\text{cr},1}$ , the evolution of the shocked region approaches the Blandford–McKee (BM) self-

similar form (Blandford & McKee 1976). When the blast wave arrives at  $R_0$ , it feels stronger resistance from the denser medium, and new forward and reverse shocks are formed. There are four separate regions: an unshocked high-density outer shell, a forward-shocked outer shell, a reverse-shocked inner shell, and an unshocked hot inner shell, marked as 1, 2, 3, 4, respectively. The main difference with Phase I is that region 4 is hot, leading to the different equations of the jump conditions (Dai & Lu 2002; Zhang & Mészáros 2002). The second pulse is produced by the new forward shock near  $R_0$  because its luminosity decreases with radius.

## 3. Constraining Density Structure from Double-peaked FRB Pulses

The energy and duration of the magnetar flare are denoted as  $E$  and  $\delta t$ , respectively. In Phase I, the reverse-shock crossing time is  $t_{\text{cr},1} \simeq \delta t$ . Before crossing, the Lorentz factor of the shocked region is  $\Gamma_1(t \leq t_{\text{cr},1}) = (f_1 \Gamma_{\text{ej}}^2 / 4)^{1/4}$  (Sari & Piran 1995), where  $f_1 \equiv E / (4\pi r^2 m_p n_0 c^3 \delta t \Gamma_{\text{ej}}^2)$ , and  $\Gamma_{\text{ej}}$  is the initial Lorentz factor of the ejecta. Because  $t_{\text{cr},1} = R_{\text{cr},1} / (2\Gamma_{\text{cr},1}^2 c)$ , the crossing radius  $R_{\text{cr},1}$  can be obtained:

$$R_{\text{cr},1} = \left( \frac{E \delta t}{4\pi m_p c n_0} \right)^{1/4} = 3.55 \times 10^{11} E_{40}^{1/4} \delta t_{-3}^{1/4} n_{0,3}^{-1/4} \text{ cm}. \quad (2)$$

The Lorentz factor at crossing radius is then  $\Gamma_{\text{cr},1} = (R_{\text{cr},1} / (2c\delta t))^{1/2}$ . After crossing, the shock enters the BM self-similar evolution stage that implies  $\Gamma \propto r^{-3/2}$ . Thus, a smooth transition at  $R_{\text{cr},1}$  indicates

$$\Gamma_1(t > t_{\text{cr},1}) = \Gamma_{\text{cr},1} (r / R_{\text{cr},1})^{-3/2}. \quad (3)$$

The BM evolution of Phase I suddenly ends as the blast wave encounters the density jump at  $R_0$ . From observations we gather that the time separation between the two pulses is  $\Delta T = 28.91$  ms, thus we can determine  $R_0$  by letting

$$\Delta T = \int_{R_{\text{cr},1}}^{R_0} \frac{dr}{2\Gamma_1^2 c}. \quad (4)$$

Then we get

$$R_0 = R_{\text{cr},1} \left( \frac{4\Delta T}{\delta t} + 1 \right)^{1/4}. \quad (5)$$

As region 4 is hot, the jump conditions between region 3 and 4 are (Dai & Lu 2002; Zhang & Mészáros 2002)

$$\left( \frac{n_3}{n_4} \right)^2 = \frac{(e_3/e_4)(1 + 3e_3/e_4)}{3 + e_3/e_4}, \quad (6)$$

$$\gamma_{34}^2 = \frac{(1 + 3e_3/e_4)(3 + e_3/e_4)}{16e_3/e_4}, \quad (7)$$

where  $e$ ,  $n$  are energy density and particle number density, and  $\gamma_{34}$  is the relative Lorentz factor between region 3 and 4. The initial Lorentz factor of region 4 is  $\gamma_4 = \Gamma_1(R_0)$ . Defining  $f \equiv e_4 / (n_1 m_p c^2)$  and combining the density-jump equations of region 1 and 2, the solution corresponding to a relativistic

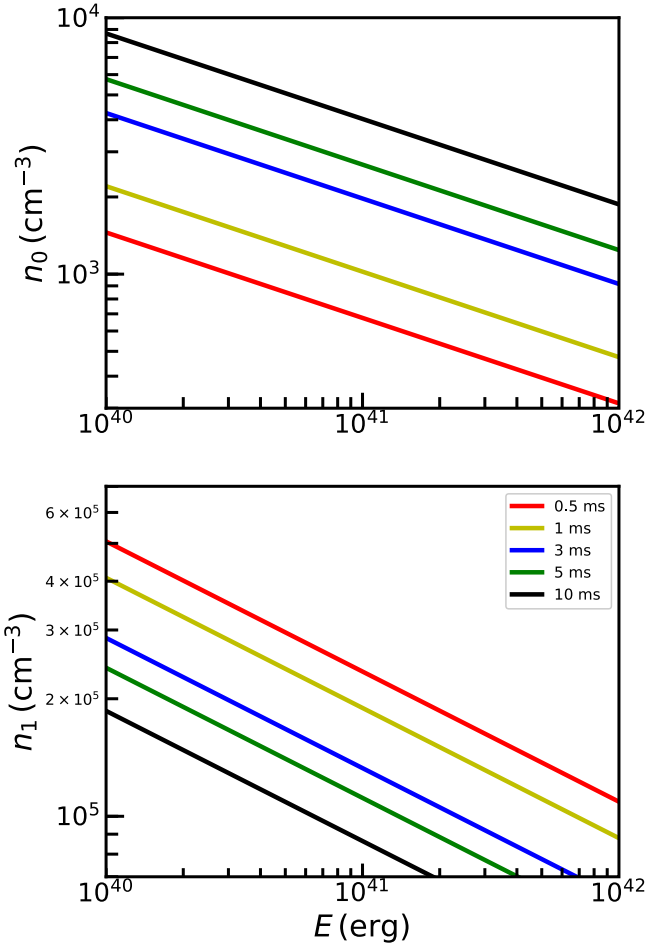


**Figure 2.** Numerically solved densities  $n_0$ ,  $n_1$  for different flare parameter sets  $E$ ,  $\delta t$ . The different colored lines correspond to different adopted  $\delta t$ , which is illustrated in the upper-right corner of the bottom panel. The behavior of  $n_0$ ,  $n_1$  matches Equations (17), (18) well. The maser efficiency  $f_{\xi_{\text{II}}} = 5 \times 10^{-2}$  is assumed and  $f_{\xi_1}$  is obtained according to Equation (11). For the typical parameters of our interest, the requirement of a relativistic reverse shock is always fulfilled.

reverse shock is (Dai & Lu 2002)

$$\gamma_2 = \gamma_3 = \frac{\gamma_4^{1/2} f^{1/4}}{3^{1/4}}, \quad (8)$$

$$\gamma_{34} = \frac{3^{1/4} \gamma_4^{1/2}}{2f^{1/4}} \gg 1. \quad (9)$$

The above solution requires the density-jump ratio  $n_1/n_0 > 64/3$  and this will be justified later for the case of FRB 200428.

Now we can deduce the densities  $n_0$ ,  $n_1$  from pulse properties. From observation we know that pulse I of FRB 200428 was detected only by CHIME, and that pulse II was detected simultaneously by CHIME and STARE2. Pulse II is found to be much more luminous than pulse I (Bochenek et al. 2020; The CHIME/FRB Collaboration et al. 2020). Here we scale the luminosity ratio as  $\sim 10$ . Because the shock luminosity is  $L_{\text{sh}} \simeq 4\pi r^2 \Gamma^4 n m_p c^3$ , the peak FRB luminosity can be obtained as  $\nu L_{\nu}|_{\text{pk}} \simeq f_{\xi} L_{\text{sh}}$ , where  $f_{\xi}$  is the maser

efficiency. Then the luminosity ratio of two peaks is

$$\begin{aligned} \frac{\nu L_{\nu}|_{\text{pk,II}}}{\nu L_{\nu}|_{\text{pk,I}}} &\sim \frac{f_{\xi_{\text{II}}} 4\pi R_0^2 n_1 \gamma_2 (R_0)^4 m_p c^3}{f_{\xi_1} 4\pi R_{\text{cr,I}}^2 n_0 \Gamma_{\text{cr,I}}^4 m_p c^3} \\ &\simeq \frac{4}{3} \left( \frac{R_0}{R_{\text{cr,I}}} \right)^{-4} \frac{f_{\xi_{\text{II}}}}{f_{\xi_1}}, \end{aligned} \quad (10)$$

therefore

$$\frac{f_{\xi_{\text{II}}}}{f_{\xi_1}} = 7.5 \left( \frac{\nu L_{\nu}|_{\text{pk,II}}}{\nu L_{\nu}|_{\text{pk,I}}} \right)_1 \left( \frac{4\Delta T}{\delta t} + 1 \right). \quad (11)$$

PIC simulations suggest that  $f_{\xi}$  depends strongly on the upstream magnetization parameter  $\sigma$ , and  $f_{\xi} \sim 7 \times 10^{-4}/\sigma^2$  for  $\sigma \geq 1$  (Plotnikov & Sironi 2019). For typical flare duration  $\delta t \sim 1$  ms, Equation (11) implies that  $f_{\xi_1} \ll f_{\xi_{\text{II}}}$ , thus  $\sigma_1 > 1$  is always expected. For instance, if we assume that the outer shell has  $\sigma_{\text{II}} \sim 0.1$  that corresponds to a maximum maser efficiency of  $f_{\xi_{\text{II}}} \sim 0.05$ , then  $f_{\xi_1} \sim 5.7 \times 10^{-5}$  and  $\sigma_1 \sim 3.5$ . This makes sense because the inner shell should have higher magnetization (Beloborodov 2020).

The peak frequency for synchrotron maser emission is  $\nu_{\text{pk}} = (3/2\pi)\Gamma\omega_p \max[1, \sqrt{\sigma}]$  (Plotnikov & Sironi 2019), where  $\omega_p = (4\pi n_e e^2/m_e)^{1/2}$  is the plasma frequency. However, the observed FRB frequency is shifted to a higher value due to absorption of low-energy photons by induced Compton scattering (ICS). The optical depth of ICS near  $\nu_{\text{pk}}$  is approximated as (Lyubarsky 2008; Metzger et al. 2019)

$$\begin{aligned} \tau(\nu_{\text{pk}}) &\simeq \frac{1}{10} \frac{3}{64\pi^2} \frac{\sigma_{\text{T}} \text{ctn}}{m_e} \frac{\partial}{\partial \nu} \left( \frac{L_{\nu}}{\nu} \right) \Big|_{\text{pk}}, \\ &\simeq \frac{3}{640\pi^2} \frac{\sigma_{\text{T}} \nu L_{\nu}|_{\text{pk}} \text{ctn}}{m_e \nu_{\text{pk}}^3 r^2}, \end{aligned} \quad (12)$$

where the Thompson cross section  $\sigma_{\text{T}} = 8\pi e^4/(3m_e^2 c^4)$ . Substituting  $\nu L_{\nu}|_{\text{pk}}$  into Equation (12), we obtain

$$\tau(\nu_{\text{pk}}) \simeq \frac{\pi^2 m_p}{1620 m_e} f_{\xi} \nu_{\text{pk}} t. \quad (13)$$

The observed FRB frequency  $\nu_{\text{max}}$  is reached as  $\tau \simeq 3$ . Because  $\tau(\nu) \propto \nu^{-4}$ , we get

$$\frac{\nu_{\text{max}}}{\nu_{\text{pk}}} \simeq 7.81 \left( \frac{\tau}{3} \right)^{-1/4} f_{\xi,-3}^{1/4} \left( \frac{\nu_{\text{pk}}}{\text{GHz}} \right)^{1/4} t_{-3}^{1/4}, \quad (14)$$

where the peak frequencies of two pulses

$$\nu_{\text{pk,I}} = 3\Gamma_1 \omega_{\text{p,I}} \sqrt{\sigma_1} / 2\pi, \quad \nu_{\text{pk,II}} = 3\gamma_2 \omega_{\text{p,II}} / 2\pi. \quad (15)$$

Here we implicitly take  $\sigma_{\text{II}} < 1$ . This is because the effective maser efficiency of pulse I should not be too small, as observationally the flux ratio between radio and X-ray band is  $F_{\text{radio}}/F_{\text{X}} \sim 10^{-6}$ – $10^{-5}$  (Mereghetti et al. 2020). The observed emission frequency is higher for pulse II, and according to the waterfall plots we normalize them as  $\nu_{\text{max,I}} = 400$  MHz,

$\nu_{\text{max,II}} = 1.4$  GHz. Thus

$$\begin{aligned}\nu_{\text{pk,I}} &\simeq 0.092 \left(\frac{\tau}{3}\right)^{1/5} f_{\xi_{\text{I}},-3}^{-1/5} \left(\frac{\nu_{\text{max,I}}}{400 \text{ MHz}}\right)^{4/5} t_{\text{I},-3}^{-1/5} \text{ GHz}, \\ \nu_{\text{pk,II}} &\simeq 0.253 \left(\frac{\tau}{3}\right)^{1/5} f_{\xi_{\text{II}},-3}^{-1/5} \left(\frac{\nu_{\text{max,II}}}{1.4 \text{ GHz}}\right)^{4/5} t_{\text{II},-3}^{-1/5} \text{ GHz}.\end{aligned}\quad (16)$$

These two peaks are produced at time  $t_{\text{I}} \simeq \delta t$  and  $t_{\text{II}} \simeq \delta t + \Delta T$ , respectively. Substituting into Equation (16) and combining Equations (3), (8), (15), we can obtain  $n_0, n_1$  as

$$n_0 = 3.23 \times 10^3 E_{40}^{-1/3} \delta t_{-3}^{7/15} f_{\xi_{\text{I}},-3}^{2/15} \text{ cm}^{-3}, \quad (17)$$

$$\begin{aligned}n_1 &= 5.27 \times 10^6 n_0^{-1/2} E_{40}^{-1/2} \delta t_{-3}^{7/10} f_{\xi_{\text{II}},-3}^{-4/5} \\ &\times \left(\frac{4\Delta T}{\delta t} + 1\right)^{3/2} \left(\frac{\Delta T}{\delta t} + 1\right)^{-4/5} \text{ cm}^{-3}.\end{aligned}\quad (18)$$

The above expression for  $n_1$  is valid only if  $\gamma_2 > 1$ . In the situation of  $\gamma_2 \simeq 1$ , from Equations (15), (16) we get

$$n_1 = 8.82 \times 10^7 \delta t_{-3}^{-2/5} f_{\xi_{\text{II}},-3}^{-2/5} \left(\frac{\Delta T}{\delta t} + 1\right)^{-2/5} \text{ cm}^{-3}. \quad (19)$$

The dependence of  $n_0, n_1$  on flare parameters  $E, \delta t$  is shown in Figure 2. We adopt five typical values of  $\delta t$ , and the behavior of  $n_0, n_1$  follows Equations (17), (18). From the figure we can see that, for the parameter space of our interest,  $n_1/n_0 > 64/3$  is always ensured and a relativistic reverse shock in Phase II is expected. This can be understood from the ratio of peak frequencies of two pulses:

$$\frac{\nu_{\text{pk,II}}}{\nu_{\text{pk,I}}} = \frac{1}{\sqrt{\sigma_{\text{I}}}} \frac{\gamma_2 n_1^{1/2}}{\Gamma_{\text{cr,I}} n_0^{1/2}} < \frac{1}{\sqrt{\sigma_{\text{I}}}} \frac{\gamma_4}{\Gamma_{\text{cr,I}}} \left(\frac{n_1}{n_0}\right)^{1/2}. \quad (20)$$

From Equation (16) we know  $\nu_{\text{pk,II}}/\nu_{\text{pk,I}} \sim$  a few, thus

$$\frac{n_1}{n_0} \gg \sigma_{\text{I}} \left(\frac{4\Delta T}{\delta t} + 1\right)^{3/4} \quad (21)$$

Usually with typical parameters  $n_1/n_0 > 64/3$  is always satisfied. This validates the expressions of Equation (8), (9).

The reverse-shock crossing radius in Phase II can be evaluated as follows. The initial total particle number in region 4 is the swept-up inner shell before  $R_0$ , i.e.,  $N_4 = 4\pi R_0^3 n_0/3$ . The total number in region 3 during crossing is  $N_3(r) = \int_{R_0}^r 4\pi r^2 n_4 \gamma_{34} \beta_{34} / (\gamma_3 \beta_3) dr$  (Dai & Lu 2002). During crossing, region 4 expands adiabatically so  $n_4(r) = 4\gamma_4 n_0 (r/R_0)^{-3}$ . At the crossing radius  $R_{\text{cr,II}}$  we should have  $N_3(R_{\text{cr,II}}) = N_4$ . Substituting Equations (8), (9) we obtain

$$R_{\text{cr,II}} = R_0 \left(1 + \frac{2}{3^{3/2}} n_0^{1/2} n_1^{-1/2}\right)^{1/2}. \quad (22)$$

The crossing time is then

$$t_{\text{cr,II}} = \int_{R_0}^{R_{\text{cr,II}}} \frac{dR}{2\gamma_2^2 c}. \quad (23)$$

For the fiducial values  $E = 10^{40}$  erg,  $\delta t = 1$  ms, we get  $R_0 = 9.58 \times 10^{11}$  cm,  $R_{\text{cr,II}} = 9.71 \times 10^{11}$  cm and  $t_{\text{cr,II}} = 19.6$  ms. The total mass of the baryonic shell is  $M = M_{\text{in}} + M_{\text{out}} \sim (4/3)\pi m_p [R_0^3 n_0 + (R_{\text{cr,II}}^3 - R_0^3) n_1] \simeq 1.21 \times 10^{17}$  g, which is reasonably smaller than the ejected mass of 2004 giant flare from SGR 1806-20 (Gelfand et al.

2005). The mass ratio of the two shells is  $M_{\text{out}}/M_{\text{in}} \sim 8$ , while the initial velocity ratio is approximated as  $v_{\text{out}}/v_{\text{in}} \sim R_0/R_{\text{cr,I}} \sim 3$ . Therefore, our scenario is consistent with the power-law mass distribution  $m(v) \propto v^\xi$  with  $\xi \sim 2$  if mass distribution is shaped by gravity (Beloborodov 2020). Note that the mass ejection by magnetar flares is concentrated in short episodes. The ejection rate is not well known and the slower shell might be ejected earlier. In this case, the faster shell would catch up and interact with the slower shell. The interaction of two shells could also lead to a density jump, and this has been discussed both analytically and numerically in the context of stellar winds (Luo & McCray 1991; Dwarkadas & Balick 1998; Ramirez-Ruiz et al. 2001). However, a jump ratio of  $>20$  may be not very common because observationally the upward drifting of FRBs is rarer than downward drifting, and until now only appeared for FRB 200428 and FRB 190611 (Day et al. 2020).

#### 4. The Associated X-Ray Burst

For magnetized shocks, the electrons are likely to be heated to a thermal distribution, with a mean Lorentz factor  $\bar{\gamma} \sim (1/2)(m_p/m_e)\Gamma$  (Giannios & Spitkovsky 2009). Therefore, in Phase I, the typical synchrotron frequency after crossing ( $t \geq \delta t$ ) is

$$h\nu_{\text{syn,I}} = h \frac{\bar{\gamma}^2 eB}{2\pi m_e c} \Gamma_{\text{I}} = 5.94 \text{ MeV } \sigma_{1,0}^{1/2} E_{40}^{1/2} t_{-3}^{-3/2}, \quad (24)$$

where the post-shock magnetic field strength is  $B = (64\pi\sigma_{\text{I}}\Gamma^2 m_p c^2 n)^{1/2}$ . The cooling frequency is

$$\begin{aligned}h\nu_{\text{c,I}} &= h \frac{\gamma_c^2 eB}{2\pi m_e c} \Gamma_{\text{I}} = h \frac{eB}{2\pi m_e c} \Gamma_{\text{I}} \left(\frac{6\pi m_e c}{\sigma_{\text{I}} \Gamma_{\text{I}} B^2 t}\right)^2 \\ &= 11.69 \text{ keV } \sigma_{1,0}^{-3/2} E_{40}^{-1/6} f_{\xi_{\text{I}},-3}^{-2/15} \delta t_{-3}^{-7/15} t_{-3}^{-1/2}.\end{aligned}\quad (25)$$

Initially  $\nu_{\text{syn,I}} > \nu_{\text{c,I}}$ , so fast cooling is expected. Letting  $\nu_{\text{syn,I}} = \nu_{\text{c,I}}$ , the transition time to slow cooling is

$$t_c \simeq 0.5 \text{ s } \sigma_{1,0}^2 E_{40}^{2/3} f_{\xi_{\text{I}},-3}^{2/15} \delta t_{-3}^{7/15}. \quad (26)$$

The observing X-ray band is  $\nu_X \sim 20\text{--}200$  keV, and from Equations (24), (25) we know initially  $\nu_{\text{c,I}} < \nu_X < \nu_{\text{syn,I}}$ . The observed synchrotron luminosity is then  $\nu L_{\nu,\text{syn}} \propto (\nu_X/\nu_{\text{syn,I}})^{1/2}$ . As  $\nu_{\text{syn,I}}$  decreases with time, the X-ray luminosity increases until  $\nu_{\text{syn,I}} \simeq \nu_X$ . The delay of X-ray peak arrival time with respect to radio peak ( $\sim$ several ms, Mereghetti et al. 2020) is expected. During phase II, regions 2, 3, and 4 are hot and their synchrotron emission can be significant. For region 4, its emission is brightest at  $R = R_0$  where  $N_4$  is at its maximum. Because  $\nu_{\text{syn,I}} \propto \Gamma^4$ , we have

$$\frac{h\nu_{\text{syn,4}}}{h\nu_{\text{syn,I}}(t_{\text{cr,I}})} = \frac{\gamma_4^4}{\Gamma_{\text{cr,I}}^4} = \left(\frac{R_0}{R_{\text{cr,I}}}\right)^{-6}. \quad (27)$$

Substituting Equations (5), (24) we obtain

$$h\nu_{\text{syn,4}} = h\nu_{\text{syn,I}}(\delta t) \left(\frac{4\Delta T}{\delta t} + 1\right)^{-3/2}. \quad (28)$$

Furthermore, the synchrotron frequencies of region 2 and 3 are, respectively,

$$\begin{aligned} \frac{h\nu_{\text{syn},2}}{h\nu_{\text{syn},4}} &= \frac{\gamma_2^4 \sqrt{\sigma_{\text{II}} n_1}}{\gamma_4^4 \sqrt{\sigma_{\text{I}} n_0}} = \frac{4}{3} \sqrt{\frac{n_0 \sigma_{\text{II}}}{n_1 \sigma_{\text{I}}}} \left(\frac{R}{R_0}\right)^{-4}, \\ \frac{h\nu_{\text{syn},3}}{h\nu_{\text{syn},4}} &= \frac{\gamma_3^4 \sqrt{n_4}}{\gamma_4^4 \sqrt{n_0}} = \frac{8\sqrt{\gamma_4}}{3} \frac{n_0}{n_1} \left(\frac{R}{R_0}\right)^{-11/2}, \end{aligned} \quad (29)$$

The emission from these two regions is brightest near  $R_0$  as the shock luminosity  $L_{\text{sh,II}} \propto R^2 \gamma_2^4 \propto R^{-2}$ , which means that the emission of regions 2, 3, and 4 reaches the maximum almost simultaneously in the local frame. However, in the observer frame they will be detected at different times. The emission of region 4 will arrive first because  $\gamma_4 > \gamma_2 = \gamma_3$ . The delay time of region 2 and 3 is estimated as

$$\Delta t_{2,3} \sim \int_{R_0}^{R_{\text{cr,II}}} \frac{dR}{2c} \left( \frac{1}{\gamma_2^2} - \frac{1}{\gamma_4^2} \right). \quad (30)$$

For typical values  $E = 10^{40}$  erg and  $\delta t = 1$  ms we get  $\Delta t_{2,3} \sim 18$  ms, being marginally consistent with the time interval between the second and third peak in HXMT and INTEGRAL X-ray light curves (Li et al. 2020; Mereghetti et al.

2020). Moreover, it is possible to adjust parameters  $E$ ,  $\delta t$ ,  $\sigma_{\text{I}}$ ,  $\sigma_{\text{II}}$  to make sure that  $h\nu_{\text{syn},1}$ ,  $h\nu_{\text{syn},2}$ ,  $h\nu_{\text{syn},4}$  are in the observing band.

Nevertheless, there are two discrepancies in the X-ray observations. First, from Equations (27), (29) we know  $h\nu_{\text{syn},2} < h\nu_{\text{syn},4} < h\nu_{\text{syn},1}$ . However, the peak energy of three peaks in INTEGRAL light curve seems to increase with time (Mereghetti et al. 2020). This problem will be alleviated if nonthermal electrons are present in the downstream and the superposition of two components could change the peak energy of the observed spectrum. On the one hand, the nonthermal component of the FRB-associated X-ray burst has been identified observationally (Li et al. 2020). On the other hand, nonthermal acceleration of electrons by magnetized shocks in the presence of ions has been verified in PIC simulations (Amato & Arons 2006). The second inconsistency is that the shock luminosity in Phase I is higher than that of Phase II, so the first X-ray peak is expected to be brighter than the second one. Observationally, however, it is the second peak that has the highest luminosity. This contradiction can be reconciled if an efficiency parameter is introduced. PIC simulations show that the nonthermal acceleration efficiency varies with magnetization and number fraction of ions (Amato & Arons 2006). Therefore, we should expect different X-ray radiation efficiencies of Phase I and II. The fitting of X-ray bursts properties needs additional free parameters, and therefore is left for future work. Moreover, the observed X-ray flux should contain thermal emission from the magnetar, and thus can be merely considered as an upper limit for shock downstream emission.

## 5. Discussion and Conclusions

In this work, we have focused on the temporal behavior of FRB 200428, and the production of two pulses is ascribed to the shock propagation in a stratified medium. Because the second pulse has a higher frequency, a jump from a low-density shell to a high-density shell is expected. Both the luminosity

and peak frequency of FRB emission can be well explained in the synchrotron maser scenario, assuming typical flare parameters. The density of two shells can be determined self-consistently. Synchrotron emission of different post-shock regions are in the X-ray band and can be responsible for a portion of FRB-associated X-ray burst fluence. Moreover, the arrival times of three peaks of the X-ray bursts could match the model prediction well.

Several previous works have discussed the application of the synchrotron maser model to FRB 200428 (Margalit et al. 2020; Wu et al. 2020; Yu et al. 2020); however, none of them have explained how double peaks can be formed. On the contrary, Lu et al. (2020) and Wang (2020) attributed these two peaks to two separated ejectas, and they place strong constraints on this scenario. Contrary to their assumption, only one ejecta exists in our scenario, and it is the density jump that leads to two pulses. The recurrence of a double-peaked character (Kirsten et al. 2020) favors our scenario, because one should not expect the magnetar to produce multiple ejectas during each flare.

Alternatively, a few works have proposed that coherent curvature emission could be responsible for FRB 200428 (Dai 2020; Geng et al. 2020; Lu et al. 2020; Wang et al. 2020; Yang et al. 2020). For this mechanism, coherence is achieved if the phases of EM waves emitted by each individual electron in the magnetosphere are near the same (Ginzburg & Zhelezniakov 1975; Benford & Buschauer 1977). Lu et al. (2020) and Yang et al. (2020) assumed that a disturbance from the magnetar surface spreads and launches Alfvén waves into the polar region. In their scenario, the NS surface is heated precedently and X-rays should appear earlier than FRB pulses, as an FRB is not produced until Alfvén waves reach the charge starvation radius. This inconsistency with the observation also applies to the magnetar-asteroid model of Geng et al. (2020), but not to Dai (2020) as coherent curvature emission occurs before the asteroid matter is accreted onto the magnetar. However, the third X-ray peak in INTEGRAL and Insight-HXMT light curves are not expected in any of these models.

The structure of the baryonic shell is expected to be ubiquitous because the mass outflow is unsteady during magnetar flares. Once it has been upgraded properly, this density-jump scenario can potentially be applied to FRBs with multiple pulses. We note that the pulse properties depend strongly on the external medium in synchrotron maser models (Metzger et al. 2019; Beloborodov 2020). Therefore, different density structures can lead to a variety of FRB light curves. Other kinds of density structures can be considered for individual FRBs in the future, which is analogous to afterglow modeling in gamma-ray burst studies.

This work is supported by the National Key Research and Development Program of China (grant No. 2017YFA0402600) and the National Natural Science Foundation of China (grant No. 11833003, 11903018, and 11851305). D.X. is also supported by the Natural Science Foundation for the Youth of Jiangsu Province (grant No. BK20180324).

## ORCID iDs

Di Xiao  <https://orcid.org/0000-0002-4304-2759>

## References

Alsop, D., & Arons, J. 1988, *PhFl*, 31, 839

- Amato, E., & Arons, J. 2006, *ApJ*, 653, 325
- Bannister, K. W., Deller, A. T., Phillips, C., et al. 2019, *Sci*, 365, 565
- Beloborodov, A. M. 2017, *ApJL*, 843, L26
- Beloborodov, A. M. 2020, *ApJ*, 896, 142
- Benford, G., & Buschauer, R. 1977, *MNRAS*, 179, 189
- Blandford, R. D., & McKee, C. F. 1976, *PhFI*, 19, 1130
- Bochenek, C. D., Ravi, V., Belov, K. V., et al. 2020, *Natur*, 587, 59
- CHIME/FRB Collaboration, Amiri, M., Bandura, K., et al. 2019a, *Natur*, 566, 235
- CHIME/FRB Collaboration, Amiri, M., Andersen, B. C., et al. 2020, *Natur*, 582, 351
- CHIME/FRB Collaboration, Andersen, B. C., Bandura, K., et al. 2019b, *ApJL*, 885, L24
- Chittidi, J. S., Simha, S., Mannings, A., et al. 2020, arXiv:2005.13158
- Cordes, J. M., & Chatterjee, S. 2019, *ARA&A*, 57, 417
- Cruces, M., Spitler, L. G., Scholz, P., et al. 2020, arXiv:2008.03461
- Dai, Z. G. 2020, *ApJL*, 897, L40
- Dai, Z. G., & Lu, T. 2002, *ApJL*, 565, L87
- Day, C. K., Deller, A. T., Shannon, R. M., et al. 2020, *MNRAS*, 497, 3335
- Dwarkadas, V. V., & Balick, B. 1998, *ApJ*, 497, 267
- Fonseca, E., Andersen, B. C., Bhardwaj, M., et al. 2020, *ApJL*, 891, L6
- Gelfand, J. D., Lyubarsky, Y. E., Eichler, D., et al. 2005, *ApJL*, 634, L89
- Geng, J.-J., Li, B., Li, L.-B., et al. 2020, *ApJL*, 898, L55
- Giannios, D., & Spitkovsky, A. 2009, *MNRAS*, 400, 330
- Ginzburg, V. L., & Zhelezniakov, V. V. 1975, *ARA&A*, 13, 511
- Hoshino, M., & Arons, J. 1991, *PhFIB*, 3, 818
- Hoshino, M., Arons, J., Gallant, Y. A., & Langdon, A. B. 1992, *ApJ*, 390, 454
- Israel, G. L., Esposito, P., Rea, N., et al. 2016, *MNRAS*, 457, 3448
- Katz, J. I. 2018, *PrPNP*, 103, 1
- Kirsten, F., Snelders, M., Jenkins, M., et al. 2020, arXiv:2007.05101
- Kothes, R., Sun, X., Gaensler, B., & Reich, W. 2018, *ApJ*, 852, 54
- Li, C. K., Lin, L., Xiong, S. L., et al. 2020, arXiv:2005.11071
- Lorimer, D. R., Bailes, M., McLaughlin, M. A., Narkevic, D. J., & Crawford, F. 2007, *Sci*, 318, 777
- Lu, W., Kumar, P., & Zhang, B. 2020, *MNRAS*, 498, 1397
- Luo, D., & McCray, R. 1991, *ApJ*, 379, 659
- Lyubarsky, Y. 2008, *ApJ*, 682, 1443
- Lyubarsky, Y. 2014, *MNRAS*, 442, L9
- Macquart, J. P., Prochaska, J. X., McQuinn, M., et al. 2020, *Natur*, 581, 391
- Marcote, B., Nimmo, K., Hessels, J. W. T., et al. 2020, *Natur*, 577, 190
- Margalit, B., Beniamini, P., Sridhar, N., & Metzger, B. D. 2020, *ApJL*, 899, L27
- Melrose, D. B. 2017, *RvMPP*, 1, 5
- Mereghetti, S., Savchenko, V., Ferrigno, C., et al. 2020, *ApJL*, 898, L29
- Metzger, B. D., Margalit, B., & Sironi, L. 2019, *MNRAS*, 485, 4091
- Murase, K., Kashiyama, K., & Mészáros, P. 2016, *MNRAS*, 461, 1498
- Petroff, E., Barr, E. D., Jameson, A., et al. 2016, *PASA*, 33, e045
- Petroff, E., Hessels, J. W. T., & Lorimer, D. R. 2019, *A&ARv*, 27, 4
- Platts, E., Weltman, A., Walters, A., et al. 2019, *PhR*, 821, 1
- Plotnikov, I., & Sironi, L. 2019, *MNRAS*, 485, 3816
- Popov, S. B., & Postnov, K. A. 2013, arXiv:1307.4924
- Popov, S. B., Postnov, K. A., & Pshirkov, M. S. 2018, *PhyU*, 61, 965
- Prochaska, J. X., Macquart, J.-P., McQuinn, M., et al. 2019, *Sci*, 366, 231
- Rajwade, K. M., Mickaliger, M. B., Stappers, B. W., et al. 2020, *MNRAS*, 495, 3551
- Ramirez-Ruiz, E., Dray, L. M., Madau, P., & Tout, C. A. 2001, *MNRAS*, 327, 829
- Ravi, V., Catha, M., D’Addario, L., et al. 2019, *Natur*, 572, 352
- Ridnaia, A., Svinkin, D., Frederiks, D., et al. 2020, arXiv:2005.11178
- Sari, R., & Piran, T. 1995, *ApJL*, 455, L143
- Tavani, M., Casentini, C., Ursi, A., et al. 2020, arXiv:2005.12164
- Tendulkar, S. P., Bassa, C. G., Cordes, J. M., et al. 2017, *ApJL*, 834, L7
- The CHIME/FRB Collaboration, Andersen, B. C., Bandura, K. M., et al. 2020, *Natur*, 587, 54
- Wang, J.-S. 2020, *ApJ*, 900, 172
- Wang, W.-Y., Xu, R., & Chen, X. 2020, *ApJ*, 899, 109
- Waxman, E. 2017, *ApJ*, 842, 34
- Wu, Q., Zhang, G. Q., Wang, F. Y., & Dai, Z. G. 2020, *ApJL*, 900, L26
- Yang, Y.-P., Zhu, J.-P., Zhang, B., & Wu, X.-F. 2020, *ApJL*, 901, L13
- Yu, Y.-W., Zou, Y.-C., Dai, Z.-G., & Yu, W.-F. 2020, arXiv:2006.00484
- Zhang, B., & Mészáros, P. 2002, *ApJ*, 566, 712
- Zhong, S.-Q., Dai, Z.-G., Zhang, H.-M., & Deng, C.-M. 2020, *ApJL*, 898, L5
- Zhou, P., Zhou, X., Chen, Y., et al. 2020, arXiv:2005.03517